Ultrafast Harmonic Coherent Compound (UHCC) Imaging for High Frame Rate Echocardiography and Shear-Wave Elastography

Mafalda Correia, Jean Provost, Simon Chatelin, Olivier Villemain, Mickael Tanter, and Mathieu Pernot

Abstract—**Transthoracic shear-wave elastography (SWE) of the myocardium remains very challenging due to the poor quality of transthoracic ultrafast imaging and the presence of clutter noise, jitter, phase aberration, and ultrasound reverberation. Several approaches, such as diverging-wave coherent compounding or focused harmonic imaging, have been proposed to improve the imaging quality. In this study, we introduce ultrafast harmonic coherent compounding (UHCC), in which pulse-inverted diverging waves are emitted and coherently compounded, and show that such an approach can be used to enhance both SWE and high frame rate (FR) B-mode Imaging. UHCC SWE was first tested in phantoms containing an aberrating layer and was compared against pulse-inversion harmonic imaging and against ultrafast coherent compounding (UCC) imaging at the fundamental frequency. *In vivo* feasibility of the technique was then evaluated in six healthy volunteers by measuring myocardial stiffness during diastole in transthoracic imaging. We also demonstrated that improvements in imaging quality could be achieved using UHCC B-mode imaging in healthy volunteers. The quality of transthoracic images of the heart was found to be improved with the number of pulse-inverted diverging waves with a reduction of the imaging mean clutter level up to 13.8 dB when compared against UCC at the fundamental frequency. These results demonstrated that UHCC B-mode imaging is promising for imaging deep tissues exposed to aberration sources with a high FR.**

Index Terms—**Cardiac stiffness, coherent compounding, pulse-inversion (PI) harmonic imaging, shear-wave elastography (SWE), ultrafast imaging.**

I. Introduction

MYOCARDIAL stiffness evaluation could help to assess and diagnose several pathologies associated with elasticity changes, such as ischemia, cardiomyopathies, and heart failure. However, as of today, myocardial stiffness cannot be measured noninvasively in clinical practice. In the past decades,

ultrasound [1]–[7] and magnetic resonance [8]–[10] elastography imaging techniques have been proposed and developed to evaluate tissue stiffness properties. Techniques are typically based on the mapping of the propagation of mechanical waves in tissue; more specifically, low-frequency shear waves are induced and tracked to estimate their propagation speed (which typically lies between 1 and 10 m/s). Specifically, ultrasound shear-wave elastography (SWE) consists in: 1) generating a push using acoustic radiation force; 2) image the resulting shear-wave propagation; and 3) map the local velocity of the shear wave, which can be used to determine the local stiffness of tissues using rheological models of varying complexities.

Recent advances in the elastography techniques have allowed for stiffness measurements in deep organs, such as the heart [11]–[16]. Indeed, several *in vivo* SWE studies have shown in open-chest animals that local stiffness measurements, during one cardiac cycle, are feasible and clinically relevant [17]–[19]. A high imaging frame rate (FR) is required, i.e., typically above 1000 frames/s, to track shear waves induced in the human heart. Different approaches were proposed to achieve such FRs, such as, ECG gated [20], [21], and ultrafast imaging with unfocused transmit waves [22]–[26]. However, transthoracic shear-wave imaging remains challenging *in vivo* for multiple reasons. First, the presence of clutter noise, jitter, phase aberrations, and ultrasound reverberation reduce the imaging quality due to distortion of the transmitted pulses. Second, ultrasound attenuation reduces the signal-to-noise ratio (SNR) of the tissue velocities used to track the shear wave. Recent studies have shown, independently, that harmonic imaging [27] and coherent compounding [28] could palliate these two issues.

Harmonic imaging uses the nonlinear propagation of ultrasound wave to improve image quality [29]. Indeed, many factors, such as, e.g., the presence of fat, skin layer thickness, and hydration level result in the progressive distortion of ultrasound waves as they propagate into the tissue. This distortion leads to imaging artifacts, such as, e.g., clutter noise, jitter, phase aberration, and ultrasound reverberation. Harmonic imaging provided a reduction of these artifacts using a lower frequency in transmit but without compromising on contrast and resolution [30]. The nonlinear propagation of ultrasound waves, in biological tissues, generates harmonic frequencies that are multiple integers of the fundamental transmitted-wave frequency. To perform harmonic imaging, one must isolate the higher harmonic signals contained in the backscattered ultrasound echoes,

and different methods typically based on filtering and pulse inversion have been proposed to do so [30]. Indeed, a bandpass filter [31] can be directly applied onto the baseband signals to isolate the second harmonic content. In pulse-inversion (PI) techniques [32], two identical pulses of opposite polarity are sequentially transmitted. Their respective received signals are then summed, which result in the cancellation of linear and odd harmonic components and in the doubling of the even harmonic components. The PI method is often preferred as it has the advantage of cancelling harmonic content generated by the electronics. However, since two pulses are summed to form a single image, PI divides the imaging FR by 2.

While harmonic imaging techniques have been used extensively for B-mode and contrast imaging, their application to SWE is relatively recent. Song *et al.* [27] proposed a PI harmonic sequence with unfocused emissions for SWE, using a phased-array transducer to improve transthoracic cardiac shear-wave measurements. Also, Doherty *et al.* [33] proposed a fully sampled sliding-window PI harmonic technique that decreases jitter and does not divide by half the imaging FR, to arterial acoustic radiation force impulse imaging improvement. Both works showed an improvement of the tissue velocity estimation, indicating that harmonic imaging for cardiac transthoracic applications can contribute to improve shear-wave tracking and, as a consequence, myocardial stiffness measurements.

Approaches based on the coherent compounding of successive backscattered echoes, such as, e.g., as synthetic aperture imaging [34] and plane-wave coherent compounding [35], have been proposed to improve image quality and motion estimation. For instance, in plane-wave coherent compounding, the backscattered echoes from successive tilted plane waves transmitted at high FR are coherently compounded to restore a synthetic focus in transmit. Recently, this principle was extended to diverging waves [28] to achieve larger fields-of-view using ultrafast ultrasound imaging in cardiac applications. This approach is similar to synthetic aperture imaging when a small number of virtual sources positioned behind the probe are used [36].

Based on [28], we propose to combine the coherent compounding approach with harmonic imaging, using a sliding-window PI approach, with the objective of improving transthoracic ultrafast imaging of the heart. In this study, we demonstrate that by combining the two techniques, larger SNR and reduced clutter and aberration noise can be obtained.

Specifically, we propose two implementations of ultrafast harmonic coherent compound (UHCC) imaging: one for cardiac SWE, and another for high FR B-mode imaging. UHCC SWE was designed for enhanced shear-wave propagation tracking and thus is performed at a very high FR. We showed herein that UHCC SWE improves the SNR of shear-wave velocity mapping, when compared against ultrafast coherent compound (UCC) imaging at the fundamental frequency [28] and sliding-window PI harmonic (UH) imaging [33] in a porkbelly gelatin–agar phantom. The *in vivo* feasibility of UHCC SWEI was evaluated on the heart, by measuring the diastolic myocardial stiffness transthoracically of six healthy volunteers. UHCC B-mode imaging was designed to improve imaging quality at large field-of-view and high FR, and evaluated *in vivo*

in healthy volunteers. We showed that UHCC B-mode imaging is more efficient for clutter noise reduction than UCC B-mode imaging at the fundamental frequency.

II. MATERIALS AND METHODS

An Aixplorer system (Supersonic Imagine, Aix-en-Provence, France) and a 2.75-MHz linear phased-array transducer (Vermon S.A., Tours, France, 96 elements, 0.2-mm pitch) were used for B-mode and SWE acquisitions. Two sequences based on ultrafast imaging [28] were designed: a first sequence dedicated to SWE imaging, and a second to perform B-mode imaging. The two sequences were built with similar transmit patterns and were adapted according to the constraints of each imaging mode.

A. Imaging Sequences

The imaging sequences developed herein are based on the emission of diverging waves. Diverging waves are defined by a virtual source located behind the probe and are associated with an emission subaperture. These diverging waves emanating from different virtual sources can then be coherently summed, and image quality can be improved (see [28] for details).

For each imaging mode, a different diverging-waves' transmission sequence was designed. SWE requires a high FR for the tracking of the propagation of shear waves. Hence, a small number of virtual sources were used in SWE sequences. To increase the relatively limited SNR associated with a small number of virtual sources, the virtual sources can be positioned farther behind the probe to increase the radius of the diverging wave, which allows for a larger number of elements contributing to the emission and limits the geometrical attenuation. The tradeoff, however, is a reduced field-of-view. In the case of B-mode imaging, a large number of virtual sources positioned near the probe were used to achieve a large field-of-view and high contrast imaging, at the cost of a reduced FR.

To perform harmonic imaging, the emission associated with each virtual source was performed twice, with opposite polarities.

1) UHCC Imaging: A shear wave was generated using a push beam with a 2.75-MHz central frequency with full aperture, i.e., using all the 96 elements of the probe. Immediately after generating the shear wave, the UHCC imaging sequence was launched. In this sequence, N virtual sources were used with a full aperture, i.e., with all 96 elements). The set of N diverging waves was transmitted (center frequency $=$ 1.9 MHz and pulse duration $=$ 2 cycles) by organizing the virtual sources (indicated by $i = 1, \ldots, N$ in Fig. 1) in a virtual array with a pitch equal to $96/N$ elements (see Fig. 1), and at a 30-mm distance behind the probe. For each virtual source, diverging waves of opposite polarity were emitted sequentially and the backscattered RF signals associated with both polarities were recorded and summed using a sliding window [33]. Finally, by coherently recombining each harmonic data set associated with different virtual sources, compounded harmonic images were produced with an FR equal to the pulse
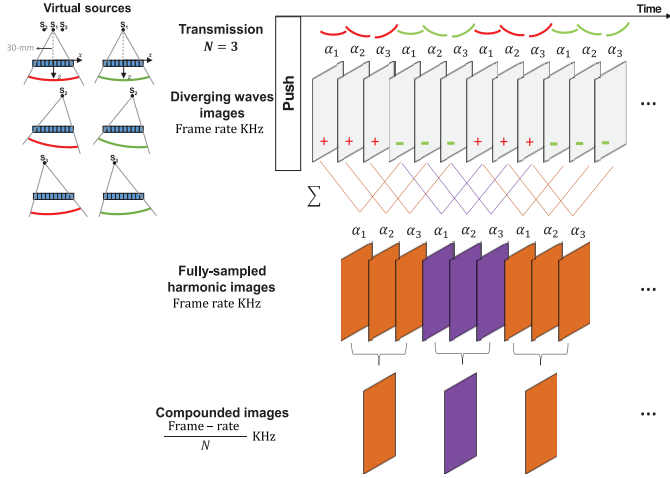
Fig. 1. UHCC SWE sequence principle. Example of implementation of a sliding-window PI harmonic technique and three coherently compounded diverging waves.
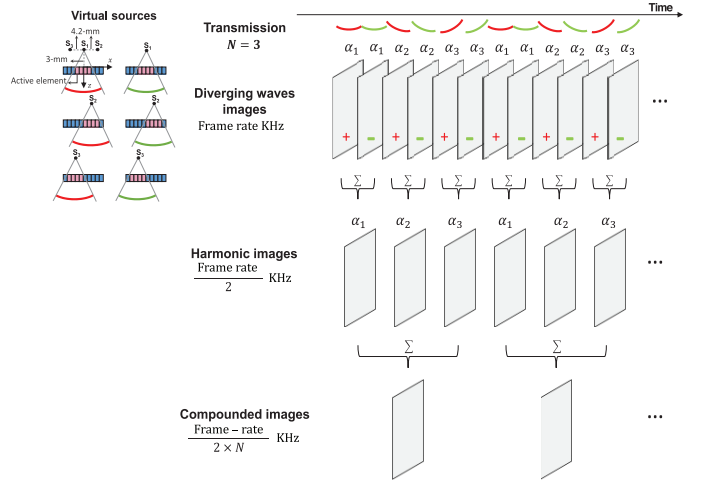

Fig. 2. UHCC B-mode sequence principle. Example of implementation of a conventional PI harmonic technique with three coherently compounded diverging waves.

repetition frequency. From these images, 2-D axial tissue displacements' maps were obtained using a table–sum 1-D RF cross correlation with cosine interpolation applied onto RF data [37], [38]. After compounding of the images associated with each virtual source, the resulting FR was, therefore, given by

$$FR = \frac{PRF}{N} \qquad (1)$$

where PRF is the pulse repetition frequency and N is the number of coherently compounded diverging waves. The FR achieved was therefore equal to the one in the UCC imaging sequence [28].

The time sequence of an UHCC SWE acquisition is summarized in Fig. 1, in which an example using three diverging waves is provided. In this study, the UHCC was compared against other previously published techniques, which correspond to UHCC without the use of either pulse inversion (UCC) or coherent compounding (UH), respectively.

2) UHCC B-Mode Imaging: For B-mode imaging, a set of N diverging waves was transmitted (center frequency = 1.9 MHz and pulse duration = 2 cycles) using a 21-element subaperture. The virtual sources were arranged in a virtual 1-D array by positioning each virtual source ($i = 1, \ldots, N$) at the center of a (96/21)-element subaperture (Fig. 2), i.e., 4.2-mm distance space, and at a 3-mm distance behind the ultrasound probe. For each virtual source, diverging waves of opposite polarity were emitted sequentially and backscattered RF signals from each polarity were received and summed. Unlike UHCC SWE sequence no sliding-window sum was applied. By coherently recombining each N-harmonic data set, compounded images were produced. The resulting FR is given by

$$FR = \frac{PRF}{2 \times N} \qquad (2)$$

where PRF is the pulse repetition frequency and N is the number of coherently compounded diverging waves. The B-mode UHCC imaging sequence is summarized in Fig. 2, using a three diverging-waves' example.
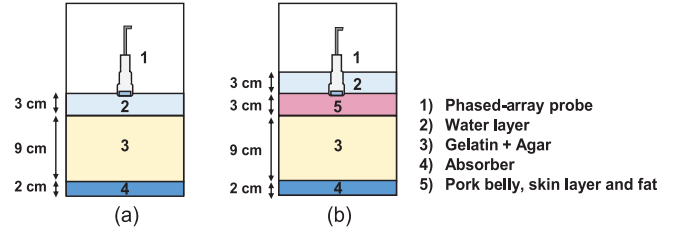
Fig. 3. *In vitro* experimental apparatus. (a) Gelatin–agar phantom configuration. (b) Pork-belly gelatin–agar phantom configuration.

B. In Vitro Experimental Setup

1) Pork-Belly Gelatin–Agar Phantom Fundamental and Harmonic Coherently Compounded Diverging-Waves' SWE Studies: Experiments to quantify the image quality of UHCC SWE were performed in a pork-belly gelatin–agar phantom (7% gelatin, 2% Agar, and 1% propanol), with two different experimental apparatuses.

In the first experimental apparatus, an absorber made of polyurethane (NPL, UK) was covered with a gelatin–agar layer to create a gelatin–agar phantom [Fig. 3(a)] that mimics an ideal homogeneous soft tissue.

In the second one, a fresh piece of pork-belly skin with fat was positioned above the gelatin–agar [Fig. 3(b)]. The pork-belly skin layer allowed us to generate ultrasound aberrations similar to the ones caused *in vivo*. In both experimental apparatus, the probe was positioned on top of the phantoms immersed in a layer of water to guarantee good acoustic coupling.

In all the *in vitro* experiments, a shear wave was generated using a 300-μs-long, 2.75-MHz push beam focused at 65 mm below the center of the transducer. Six different sequences to track the shear wave during 7 ms were compared in the two phantom configurations. Specifically, three different sequences with $N = 1, 2,$ and 3 coherently compounded diverging waves were designed, with and without pulse inversion, i.e., UHCC and UCC sequences. The imaging depth was fixed to 90 mm and the *PRF* to 5924 Hz. For the fundamental sequences

TABLE I
PARAMETERS FOR *In Vitro* UCC AND UHCC IMAGING

Imaging sequences parameters	UCC SWE imaging				UHCC SWE imaging			
	Push	UCC			Push	UHCC		
Center frequency (MHz)	2.75	2.75			2.75	1.9		
Number of pushes	$N = 1$	–			$N = 1$	–		
Number of diverging-waves transmitted (N)	–	1–3			–	2–6		
Virtual sources axial position (mm)	–	30			–	30		
Subapertures length (mm)	19.2	19.2			19.2	19.2		
Pulse-repetition-frequency (PRF)	–	5924 Hz			–	5924 Hz		
Frame rate (FR)	–	$N = 1$ 5924 Hz	$N = 2$ 2962 Hz	$N = 3$ 1975 Hz	–	$N = 2$ 5924 Hz	$N = 4$ 2962 Hz	$N = 6$ 1975 Hz
Acquisition duration	300 µs	20 ms max			300 µs	20 ms max		

(i.e., without pulse inversion), a 2.75-MHz center frequency was used. In the case of harmonic sequences, a 1.9-MHz center frequency was used in transmit and a 3.8-MHz frequency was used in receive. Each sequence was repeated five times. Additionally, prior to the shear-wave imaging sequence, a UHCC B-mode image was obtained using 10 coherently compounded diverging waves. Table I shows the UCC and UHCC SWE imaging parameters used in *in vitro*.

C. In Vivo Human Heart Experimental Setup

The *in vivo* feasibility was assessed by performing transthoracic human heart SWE and B-mode imaging in six healthy volunteers. All volunteers signed an informed consent and the research study was performed within the clinical investigation protocol no. 2015-A00187-42 approved by the CPP (Comité de Protection des Personnes), Ile de France VI, France. The acoustic output of the sequences used *in vivo* was measured using a calibrated interferometer in water. The ultrasonic sequences complied with the Food and Drug Administration (FDA) requirements (510 k Track 3, FDA) regarding the mechanical index (*MI*) and the spatial-peak time average (I_{SPTA}) with the derating factor of 0.3 dB cm^{-1} MHz^{-1}. In the SWE imaging sequence, the $MI_{0.3}$ was limited by the pressure at the focus of the push beam and it was set to 1.8. The $I_{SPTA0.3}$ was 154 mW/cm^2, assuming a repetition time of 1 s. For the unfocused transmits (80 diverging waves), the $MI_{0.3}$ and $I_{SPTA0.3}$ were 0.6 and 2.2 mW/cm^2, respectively, assuming a repetition time of 1 s. For both imaging acquisitions, $MI_{0.3}$ and $I_{SPTA0.3}$ values were inferior to $MI_{0.3} = 1.90$ and $I_{SPTA0.3} = 720$ mW/cm^2, limits imposed by the FDA. The temperature at the probe surface was also measured and remained stable for the transmission of one SWEI (20-ms duration) and B-mode imaging (15-ms duration) sequences repeated every second. The increased temperature was inferior to temperature uncertainty of the measurement system (± 0.1 °C) during the sequences' tests.

The experiments were conducted and performed by a trained cardiologist. A parasternal short-axis view was used for all the acquisitions. The time between each acquisition was 1 min. Repeatability was assessed in one volunteer by performing five successive acquisitions separated by 1 min.

1) Transthoracic UHCC SWE Study: A push beam of 2.75-MHz central frequency and 300-µs duration was induced in the center of the anteroseptal myocardial wall of the left ventricle. The focal depth was adjusted for each patient between 45 and 75 mm to position the focal zone at the midwall location of the anteroseptal wall. The UHCC SWE sequences were set to one, two, and three diverging-waves' transmission with a PRF of 6849 Hz. They were synchronized with the ECG signal to generate and detect shear-wave motion at end diastole.

A prior to the UHCC SWE acquisition, a UHCC B-mode imaging was also obtained with the following parameters: 15 diverging waves, at a 120-mm depth, and an FR equal to 153 frames/s (PRF = 4608 Hz).

2) UHCC and UCC B-Mode Imaging—Diverging Waves Coherently Compounded Number Evaluation: To evaluate the imaging quality in terms of SNR and contrast, experiments were performed using a UHCC B-mode imaging sequence and compared against the performances of UCC. For both sequences, i.e., UHCC and UCC, the transmission was performed using 1–40 coherently compounded diverging waves, at a 100-mm depth and with a PRF equal to 5319 Hz. The imaging FR varied between 5319 and 133 frames/s for the UCC sequence. For the same number of coherently compounded diverging waves, the FR was divided by two for UHCC. Table II shows the parameters used for UHCC SWEI and UHCC B-mode imaging in the *in vivo* experiments.

D. Postprocessing Analysis

Beamforming of radio-frequency (RF) signals was performed using a conventional delay-and-sum algorithm implemented on the GPU.

1) Shear-Wave Propagation Tracking and Speed Estimation: Tissue axial velocity images were obtained using 1-D cross correlation of successive frames with cosine interpolation applied on the beamformed RF signals [37], [38]. A 1.5-mm kernel size with a 97.5-% overlap was used for all sequences. Tissue velocity images were then scan converted. Spatiotemporal tissue velocity data were then computed and shear-wave speeds in the $-x$- and $+x$-directions were assessed using a linear least-squares estimation on temporal 1-D cross correlation with different lateral spatial lags (lags range: 0.2–1.8-mm) [39].

TABLE II
PARAMETERS FOR *In vivo* UHCC SWEI AND UCC/UHCC B-MODE IMAGING

Imaging sequences parameters	SWE imaging		B-mode imaging	
	Push	UHCC	UCC	UHCC
Center frequency (MHz)	2.75	1.9	2.75	1.9
Number of pushes	$N = 1$	–	–	–
Number of diverging-waves tran smitted (N)	–	2 to 6	1 to 40	2 to 80
Axial position of virtual sources (mm)	–	30	3	3
Subapertures length (mm)	19.2	19.2	4.2	4.2
Pulse-repetition-frequency (PRF)	–	6849 Hz	5319 Hz	5319 Hz
Frame rate (FR)	–	$N = 2$ 6849 Hz $N = 4$ 3425 Hz $N = 6$ 1975 Hz	$N = 1$ 5319 Hz ⋯ $N = 40$ 133 Hz	$N = 2$ 2660 Hz ⋯ $N = 80$ 67 Hz
Acquisition duration	300 µs	20 ms max	15 ms max	15 ms max

For the *in vitro* experiments, the shear-wave speed was estimated using the spatiotemporal tissue velocity data that were averaged within depths of 3-mm around the push location.

In these experiments, the SNR was evaluated quantitatively around the push region for UCC and UHCC SWE studies. SNR maps were calculated as follows:

$$\text{SNR}_{\text{dB}} = 10\log_{10} \frac{\sum_{t=0}^{T} S(x,y,z)^2}{\sigma_{xz}^2} \qquad (3)$$

where S is the tissue velocity image, σ_{xz} is the tissue velocity standard deviation in the absence of shear-wave propagation, and T is the acquisition time. The averaged SNR values were evaluated within a region-of-interest around the push location. The percentage of area within these regions-of-interest with an SNR above a threshold of 25 dB was quantified. This threshold was determined by Deffieux *et al.* [40] as an acceptable SNR for the reconstruction of shear velocity maps with a standard deviation of 10%.

For the *in vivo* acquisitions, the average myocardial wall motion was subtracted before the tissue velocity images scan conversion, since the natural myocardial wall has a low-frequency content [41], [42] and acts as a noise source in the detection of the shear-wave propagation. Also, the anteroseptal wall was segmented to using a B-mode image reference acquired.

Then, the shear-wave speed in the $-x$- and $+x$-directions was estimated, through spatiotemporal tissue velocity data that were averaged within depths of 3-mm around the push location in the anteroseptal wall. Shear-wave speeds were assessed and the adjusted coefficient of determination ($\bar{R}^2$) of the least-squares fit results was calculated. The adjusted coefficient of determination was used as an exclusion criterion for the shear-wave speed estimation. Values with an adjusted coefficient of larger than 80% of the shear-wave speed estimation were excluded and no shear-wave propagation was considered in those cases.

2) UHCC and UCC B-Mode Imaging: The B-mode image quality was assessed on the final images, i.e., after beamforming, coherent summation, scan conversion, and log compression, with a 60-dB dynamic range. Then, to evaluate imaging quality in a function of the number of diverging-waves' emitted, a mean clutter level analysis in regions-of-interest was performed, for both UHCC and UCC sequences. These regions-of-interests (5×6 mm^2) were chosen and positioned arbitrarily

in the anterior and posterior wall, and in the left ventricle cavity at approximately the same depth to evaluate the contrast of the image. For each region-of-interest, the absolute intensity values of ultrasound images were averaged over the region of interest. Finally, the mean clutter level for UHCC and UCC was determined by the ratio of the average intensity in the cardiac cavity and in the tissue.

III. RESULTS

A. Gelatin–Agar/Pork-Belly Gelatin–Agar Phantoms Fundamental and Harmonic Coherently Compounded Diverging-Waves' SWE Studies

Fig. 4 presents the results acquired for the gelatin–agar phantom. Acquisitions provided an image quality that was sufficiently high for the estimation of the shear-wave speed, regardless of the number of compounded diverging waves or of the use of pulse inversion.

Fig. 5 shows the results obtained with this pork-belly gelatin–agar phantom.

Shear-wave propagation tracking was possible for all acquisitions. However, in this case, due to the skin and fat layer, which causes ultrasound aberrations, the UHCC sequence resulted in a qualitatively larger SNR. Indeed, one can observe that the waveform is better defined with respect to the background noise and especially at larger propagation distances when using UHCC.

Figs. 6 and 7, and Table III provide a systematic and quantitative analysis of this observation. The percentage of area with an SNR above a threshold of 25 dB was quantified and is showed as well in Table III.

Fig. 6 shows that the SNR is relatively similar when using the UCC and UHCC sequences in the gelatin–agar phantom configuration. We also note that the SNR increases with the number of compounded diverging waves, as was demonstrated previously in [28].

Fig. 7, on the other hand, shows that in the presence of an aberrating layer such as a pork-belly layer and for a fixed number of compounded diverging waves, the SNR associated with UHCC is larger than the SNR associated the UCC sequence.

Table III summarizes these results using the spatial average of the SNR maps of the regions-of-interest shown in Figs. 6 and 7. Interestingly, in the absence of an aberrating layer (i.e., when using the gelatin–agar phantom), the SNR associated with
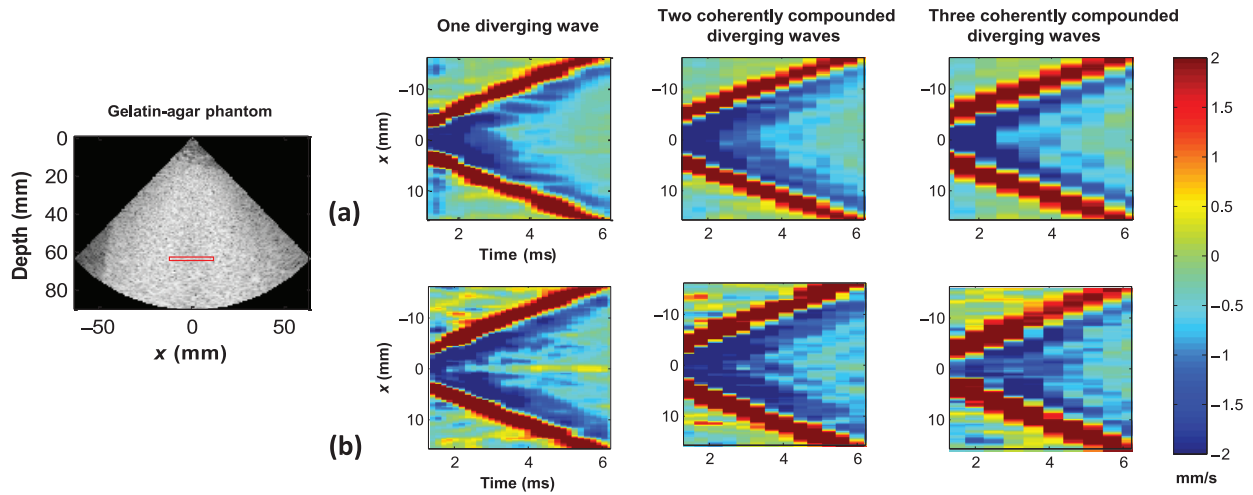
Fig. 4. Gelatin–agar phantom configuration results. An UHCC B-mode image using 10 diverging waves, spatiotemporal tissue velocity images of the shear-wave propagation (push depth equal to 65 mm) for (b) UHCC and (a) UCC SWE using one to three coherently compounded diverging waves. Tissue velocities were averaged axially within a 3-mm region.
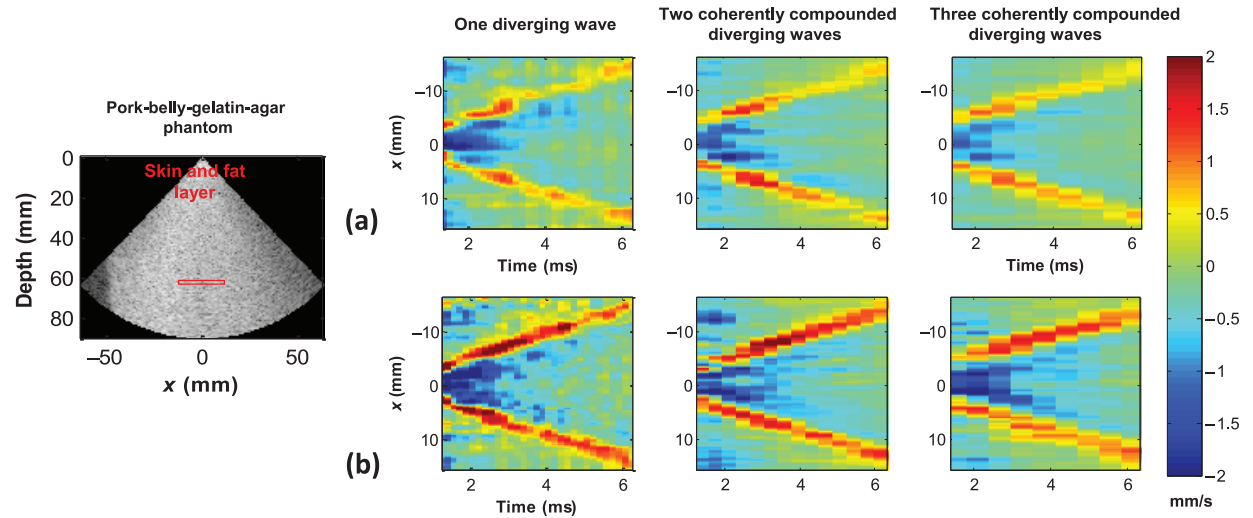

Fig. 5. Pork-belly gelatin–agar phantom configuration results. A B-mode ultrafast harmonic using 10 diverging waves and spatiotemporal tissue velocity images of the shear wave propagation (push depth 65 mm) for (a) UCC and (b) UHCC. SWE using one to three coherently compounded diverging waves. Tissue velocities were averaged axially within a 3-mm region.

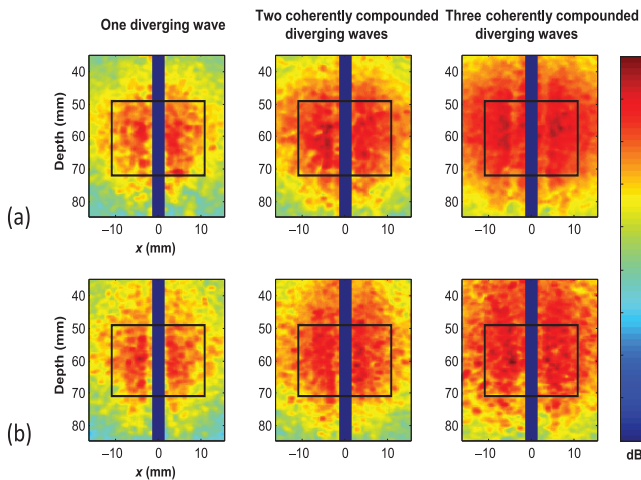**Fig. 6.** SNR maps of gelatin–agar phantom configuration for (a) UCC and (b) UHCC imaging. The blue boxes represent the push region and the black rectangles represent the SNR regions-of-interest.

Fig. 7. SNR maps of pork-belly gelatin–agar phantom configuration for (a) UCC and (b) UHCC imaging. The blue boxes represent the push region and the black rectangles represent the SNR regions-of-interest.
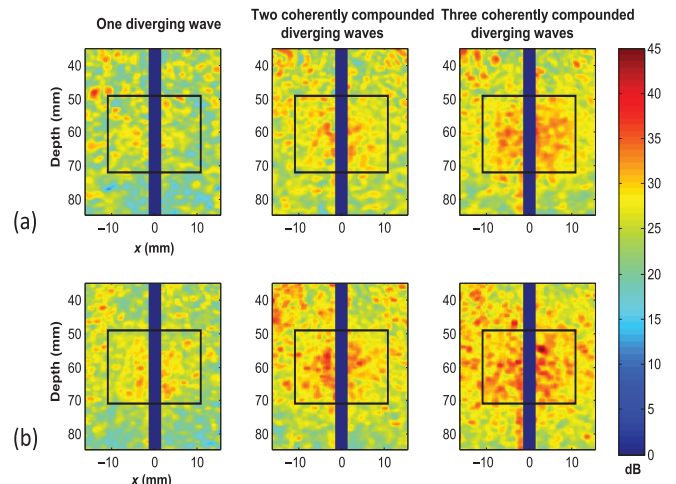
TABLE III
MEAN SNR OF UHCC AND UCC AND SNR PERCENTAGE ABOVE 25 dB IN THE REGIONS-OF-INTEREST FOR DIFFERENT NUMBER OF DIVERGING
WAVES IN THE TWO PHANTOM CONFIGURATIONS

		One diverging-wave		Two diverging-waves		Three diverging-waves	
			Area %		Area %		Area %
		SNR (dB)	> = 25 dB	SNR (dB)	> = 25 dB	SNR (dB)	> = 25 dB
Gelatin-agar phantom	Fundamental	33.7	100.0	37.2	100.0	38.7	100.0
	Harmonic	33.7	95.6	36.5	100.0	38.0	100.0
Pork-belly-gelatin-agar phantom	Fundamental	25.7	47.1	28.4	88.4	30.2	95.9
	Harmonic	27.1	69.2	30.0	96.3	32.0	99.9

the UHCC sequence was relatively equivalent with the SNR associated with the UCC sequence, albeit by a small value (0.7 dB when using two and three coherently compounded diverging waves). Also, the area above 25 dB was almost 100% using both UHCC and UCC. In contrast, the UHCC sequence provided a consistent improvement in SNR in the presence of an aberrating layer, i.e., pork-belly gelatin–agar phantom. This improvement was larger in absolute difference of SNR when increasing the number of diverging waves, but the relative improvement was approximately constant (approx. 30.6% SNR improvement when compared against UCC for a fixed number of compounded diverging waves). The SNR surface area percentage above 25 dB was higher for UHCC than UCC and increased consistently with two and three coherently compounded diverging waves.

B. In Vivo Acquisitions

1) Transthoracic UHCC SWE in the Human Heart: UHCC SWE was evaluated *in vivo* at high FRs (> 1500 frames/s), using one to three diverging waves. The spatiotemporal axial tissue displacements' images, averaged within 3-mm depth around the myocardial wall center are shown in Fig. 8 for the six volunteers.

Without coherent compounding, shear-wave imaging the shear-wave propagation was detected in volunteers 1 (in both directions), 2 (in both directions), and 6 (in $+x$-direction). Using two compounded diverging waves, the shear-wave propagation was detected in all volunteers in at least one direction. Using three diverging waves, shear waves were detected in all acquisitions in both directions, except in volunteer 6, where no shear wave was detected.

The shear-wave speed was estimated for all the acquisitions where shear waves could be tracked in at least one direction.

After the applicability of the exclusion criteria, shear-wave propagation speeds were estimated in all cases, with the exception of the volunteers 4 (in $-x$-direction) and 6 (in $-x$-direction). These results are shown in Table IV.

Repeatability tests were performed in one volunteer. The UHCC sequence was repeated five times for one to three compounded diverging and shear waves were tracked for both $-x$ and $+x$-directions. In each acquisition, spatiotemporal images

were computed, averaged within a 3-mm deep region, and centered in the left-ventricle anterior-septal midwall. Arithmetic means and standard deviations are presented in Table V.

2) Transthoracic B-Mode Human Heart Study: UHCC B-mode imaging was evaluated using 1–40 coherently compounded diverging-waves' transmission, and compared against UCC B-mode. Fig. 9 shows the imaging quality improvement of the UCC and UHCC B-mode images with an increasing number of diverging waves. As indicated by [43], increasing the number of compounded diverging waves resulted in improvements in terms of SNR, lateral resolution, and contrast when compared with a single diverging-wave image.

The mean clutter value in the cardiac cavity (regions-of-interest represented by red boxes) was also evaluated and the results are presented in Fig. 9.

The contrast of UHCC B-mode imaging was consistently larger than UCC B-mode imaging. Specifically, a clutter level decrease of 6.3 dB was found for one diverging wave and 13.8 dB for 40 diverging waves compared against UCC imaging with the same number of transmitted waves.

IV. DISCUSSION

This paper investigated the potential of a hybrid ultrafast imaging sequence based on the combination of pulse inversion and coherent compound imaging. Two sequences were designed and implemented *in vivo*: UHCC SWE and UHCC B-mode imaging. The main aim of this study was to assess the potential of UHCC as a means to improve shear-wave tracking in transthoracic cardiac applications that suffer from different noise sources.

UHCC SWE was first evaluated in an *in vitro* study. Harmonic imaging alone was shown to improve the shear-wave tracking in the presence of an aberrating layer composed of porcine fat-and-skin. Combining the coherent compounding approach allowed for a larger SNR. The feasibility of UHCC SWE was assessed in transthoracic imaging of the human heart. Experiments were performed in six healthy volunteers during end diastole in the left-ventricle anteroseptal wall. The acquisitions were performed during end diastole, i.e., when the myocardium is relatively soft and the shear-wave
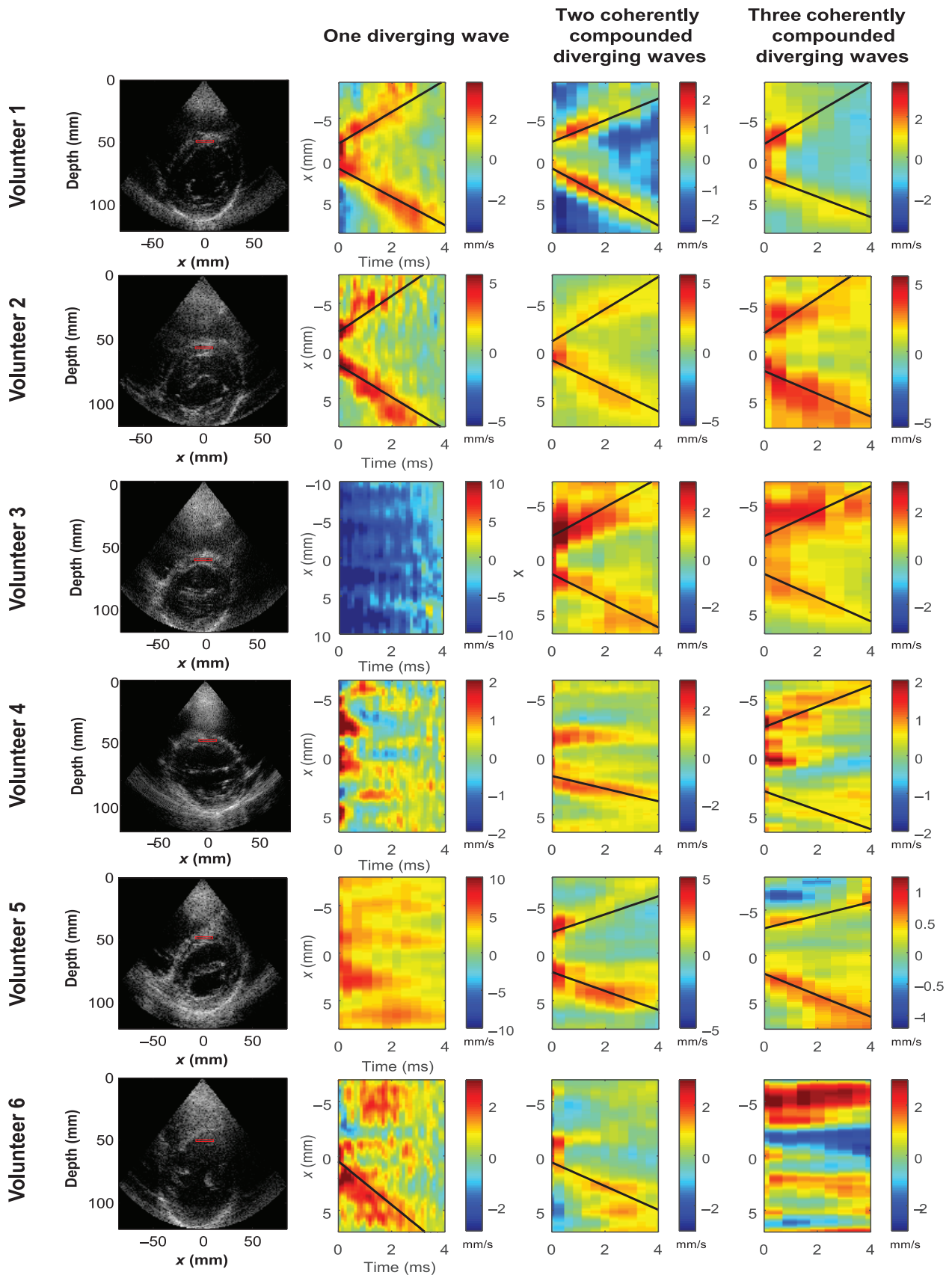
Fig. 8. *In vivo* transthoracic UHCC SWE in the human heart of six volunteers at end diastole. Left column: UHCC B-mode images acquired 5 ms before the SWE acquisition. Right column: spatiotemporal tissue velocity maps of the shear-wave propagation and averaged within 3-mm depth at the center of the myocardial wall for one (i.e., no coherent compound applied), two, and three diverging waves. The black lines represent the tracked shear-wave propagation path. Its slope corresponds to the shear-wave speed.

TABLE IV
SHEAR-WAVE SPEED ESTIMATION FOR THE SIX VOLUNTEERS

Shear wave speed ± std* (m/s)	One diverging-wave				Two diverging-waves				Three diverging-waves			
	$-x$ direction	R^2	$+x$ direction	R^2	$-x$ direction	R^2	$+x$ direction	R^2	$-x$ direction	R^2	$+x$ direction	R^2
Volunteer 1	1.65 ± 0.42	0.83	1.11 ± 0.36	0.85	1.71 ± 0.22	0.91	1.15 ± 0.26	0.89	1.92 ± 0.13	0.95	1.13 ± 0.24	0.90
Volunteer 2	1.70 ± 0.37	0.85	1.26 ± 0.51	0.80	1.75 ± 0.17	0.93	1.17 ± 0.35	0.86	1.95 ± 0.14	0.95	1.11 ± 0.39	0.84
Volunteer 3	–	–	–	–	1.34 ± 0.33	0.86	1.23 ± 0.19	0.89	1.15 ± 0.32	0.86	1.09 ± 0.16	0.93
Volunteer 4	–	–	–	–	–	–	0.54 ± 0.19	0.92	0.81 ± 0.24	0.90	0.89 ± 0.27	0.89
Volunteer 5	–	–	–	–	0.95 ± 0.13	0.84	1.39 ± 0.48	0.80	0.72 ± 0.30	0.87	1.18 ± 0.23	0.91
Volunteer 6	–	–	1.86 ± 0.38	0.84	–	–	1.09 ± 0.38	0.84	–	–	–	–

*Std denotes for standard deviation of the least-squares fit. Values with an adjusted R^2 inferior to 0.80 were excluded.

TABLE V
REPEATABILITY TEST OF SHEAR-WAVE VELOCITY MEASUREMENTS ON ONE VOLUNTEER

Shear wave speed mean ± std* (m/s)	One diverging-wave		Two diverging-waves		Three diverging-waves	
	$+x$ direction	$-x$ direction	$+x$ direction	$-x$ direction	$+x$ direction	$-x$ direction
	1.88 ± 0.51	1.64 ± 0.30	1.44 ± 0.17	1.16 + 0.20	1.59 ± 0.44	1.31 ± 0.22

*Std denotes for standard deviation of the arithmetic mean.

speed is typically in the range of 1–2 m/s. The reproducibility of the presented technique was assessed in one volunteer by performing five acquisitions. Results showed that shear-wave tracking is possible by the combination of harmonic imaging and coherent compound imaging with diverging waves. Up to three diverging waves were used. Variations between $+x$- and $-x$-directions were also found, as expected, due to the complexity and anisotropy of myocardium tissue in the anteroseptal wall, composed of an arrangement of fibers from left and right ventricles.

In this study, UHCC was shown to improve SWE in phantoms and it was feasible *in vivo* in most of the cases. However, UHCC SWE remains challenging *in vivo*, as shear-wave velocity estimation was not possible for all acquisitions. Therefore, further investigation is required to determine the ideal number of diverging-waves' transmission and to apply such technique in clinical practice routine.

The maximum number of coherently compounded diverging waves is indeed limited by the shear-wave speed. The tradeoff between the number of coherently compounded diverging waves and the temporal sampling in SWE depends on many parameters including the tissue stiffness and the probe parameters and is complex to quantify. This study suggests that for shear-wave speeds of a few meters per second, three pulse-inverted coherently compounded diverging waves (i.e., corresponding to six emissions) can be used for diastolic shear-wave propagation tracking. For a PRF of 5924 frames/s, this corresponds to an FR of 1916 frames/s.

In systole, the heart contracts and, as a result, the shear-wave speed is comparatively higher. To estimate the systolic shear-wave speed, higher FRs are required, or, equivalently, a smaller number of coherently compounded diverging waves should be used, which, in turn, reduces the SNR. The twisting of the heart during systole could also exacerbate artifacts associated with out-of-plane motion. The *in vivo* SWE studies in open-chest animals [17]–[19] have shown that shear-wave speed in systole is at least three times higher compared against the diastolic shear-wave speed (shear-wave speed in the range of 5–6 m/s). Consequently, for a PRF of 5924 frames/s, the FR necessary to track shear-wave speed in systole could reach 5924 frame/s, which corresponds to one diverging-wave transmission.

When using such a small number of emissions, it can be shown [28] that the influence of fast cardiac tissue motion degrades the coherence of the compound operation only in a limited and for most practical aspects, negligible. However, for a larger number of compounded diverging waves, a motion correction factor should be considered, as proposed previously [44].

It should also be noted that even if all the acquisitions were performed by a trained cardiologist differences between acquisitions could occurred due to patient breathing or sonographer's motion.
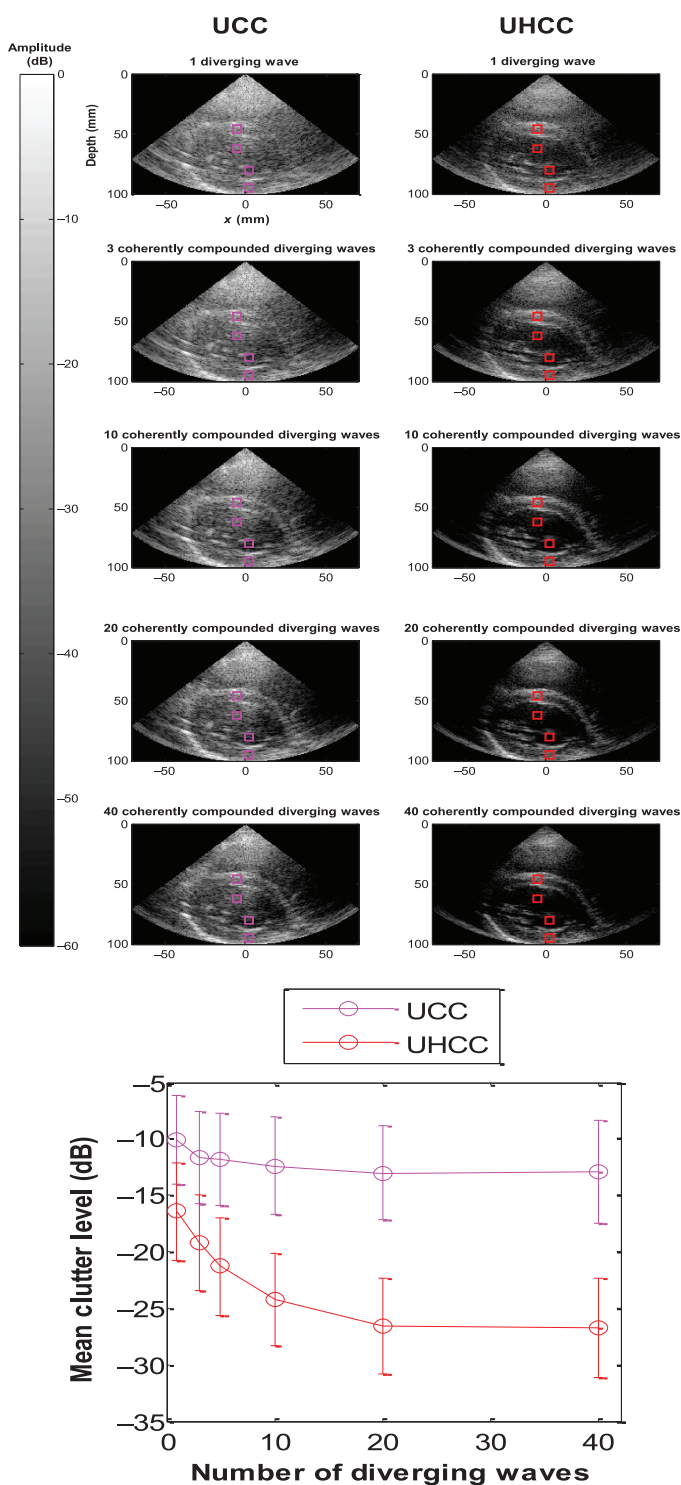
Fig. 9. UCC and UHCC B-mode images. Comparison using different number of diverging waves. The average clutter signal level was evaluated in the anterior and posterior myocardium wall and left ventricle cavity (represented by the magenta and red boxes, for UCC and UHCC, respectively).

This study was focused on the challenging application of myocardial SWE. However, UHCC could benefit and be applied to other applications that have limited imaging quality due to attenuation and aberrations, such as in liver SWE. These sequences could also be implemented in conventional linear arrays by replacing the emission of diverging waves with plane waves.

UHCC B-mode imaging was also implemented and evaluated *in vivo*. A comparison of the technique against UCC was performed to assess differences in contrast, SNR and axial resolution.

Regarding clutter noise reduction, contrast increase, and axial resolution improvement, the combination of harmonic imaging with UCC imaging allowed for a strong increase in image quality when compared against the fundamental imaging. In this method, no sliding window was applied to privilege the PI effect instead of imaging FR, unlike in the UHCC SWE sequence. Using coherent compounding, the tradeoff between FR and image quality can be adjusted at no expense in terms of field-of-view. B-mode images with good image quality can be obtained at an FR of 270 frames/s for 10 coherently compounded diverging waves and for 10 cm of depth. These results are promising for imaging deep tissues exposed to aberration sources in cardiac applications but also for the imaging of the liver in patients with high body mass index.

V. CONCLUSION

In this study, we combined harmonic imaging and coherent compounding ultrafast imaging and applied it to cardiac SWE and high FR B-mode imaging. The sequences were implemented on an ultrasound scanner and experiments were performed with a phased-array probe. Image quality and shear-wave propagation detection was evaluated by comparing the technique with the fundamental approach. Experiments performed through an aberrating layer, showed that shear-wave propagation tracking was improved by both harmonic imaging and coherent compounding and even more by the combination of both techniques, with UHCC imaging. Improvements in SNR were quantified and consistent in all *in vitro* experiments. *In vivo* feasibility was shown in the human heart to measure noninvasively shear-waves' speeds of the left ventricle wall and to evaluate B-mode image quality improvement. This technique could be used to perform shear-wave imaging and to improve B-mode imaging in the human heart.

REFERENCES

[1] M. Fatemi and J. F. Greenleaf, "Vibro-acoustography: an imaging modality based on ultrasound-stimulated acoustic emission," in *Proc. Nat. Acad. Sci. USA*, vol. 96, no. 12, pp. 6603–6608, Jun. 1999.

[2] S. Catheline, J. Thomas, F. Wu, and M. A. Fink, "Diffraction field of a low frequency vibrator in soft tissues using transient elastography," *IEEE Trans. Ultrason., Ferroelectr., Freq. Control*, vol. 46, no. 4, pp. 1013–1019, Jul. 1999.

[3] L. Sandrin *et al.*, "Transient elastography: A new noninvasive method for assessment of hepatic fibrosis," *Ultrasound Med. Biol.*, vol. 29, no. 12, pp. 1705–1713, Dec. 2003.

[4] A. P. Sarvazyan, O. V Rudenko, S. D. Swanson, J. B. Fowlkes, and S. Y. Emelianov, "Shear wave elasticity imaging: A new ultrasonic technology of medical diagnostic," *Ultrasound Med. Biol.*, vol. 24, no. 9, pp. 1419–1435, 1998.

[5] K. Nightingale, M. S. Soo, R. Nightingale, and G. Trahey, "Acoustic radiation force impulse imaging: in vivo demonstration of clinical feasibility," *Ultrasound Med. Biol.*, vol. 28, no. 2, pp. 227–235, Feb. 2002.

[6] J. Bercoff, M. Tanter, and M. Fink, "Supersonic shear imaging: a new technique for soft tissue elasticity mapping," *IEEE Trans. Ultrason., Ferroelectr., Freq. Control*, vol. 51, no. 4, pp. 396–409, Apr. 2004.

[7] P. Song, H. Zhao, A. Manduca, M. W. Urban, J. F. Greenleaf, and S. Chen, "Comb-push ultrasound shear elastography (CUSE): a novel method for two-dimensional shear elasticity imaging of soft tissues," *IEEE Trans. Med. Imag.*, vol. 31, no. 9, pp. 1821–1832, Sep. 2012.

[8] R. Muthupillai, D. Lomas, P. Rossman, J. Greenleaf, A. Manduca, and R. Ehman, "Magnetic resonance elastography by direct visualization of propagating acoustic strain waves," *Science*, vol. 269, no. 5232, pp. 1854–1857, Sep. 1995.

[9] J. Rump, D. Klatt, J. Braun, C. Warmuth, and I. Sack, "Fractional encoding of harmonic motions in MR elastography," *Magn. Reson. Med.*, vol. 57, no. 2, pp. 388–395, Feb. 2007.

[10] K. J. Glaser, A. Manduca, and R. L. Ehman, "Review of MR elastography applications and recent developments," *J. Magn. Reson. Imag.*, vol. 36, no. 4, pp. 757–774, Oct. 2012.

[11] S. J. Hsu, R. R. Bouchard, D. M. Dumont, P. D. Wolf, and G. E. Trahey, "In vivo assessment of myocardial stiffness with acoustic radiation force impulse imaging," *Ultrasound Med. Biol.*, vol. 33, no. 11, pp. 1706–1719, Nov. 2007.

[12] C. Pislaru, M. W. Urban, I. Nenadic, and J. F. Greenleaf, "Shearwave dispersion ultrasound vibrometry applied to in vivo myocardium," in *Proc. Int. Conf. IEEE Eng. Med. Biol. Soc.*, Jan. 2009, pp. 2891–2894.

[13] M. Pernot, M. Couade, P. Mateo, B. Crozatier, R. Fischmeister, and M. Tanter, "Real-time assessment of myocardial contractility using shear wave imaging," *J. Amer. Coll. Cardiol.*, vol. 58, no. 1, pp. 65–72, Jun. 2011.

[14] A. Kolipaka *et al.*, "MR elastography as a method for the assessment of myocardial stiffness: Comparison with an established pressure-volume model in a left ventricular model of the heart," *Magn. Reson. Med.*, vol. 62, no. 1, pp. 135–140, Jul. 2009.

[15] I. Sack, J. Rump, T. Elgeti, A. Samani, and J. Braun, "MR elastography of the human heart: Noninvasive assessment of myocardial elasticity changes by shear wave amplitude variations," *Magn. Reson. Med.*, vol. 61, no. 3, pp. 668–677, Mar. 2009.

[16] B. Robert, R. Sinkus, J.-L. Gennisson, and M. Fink, "Application of DENSE-MR-elastography to the human heart," *Magn. Reson. Med.*, vol. 62, no. 5, pp. 1155–1163, Nov. 2009.

[17] R. R. Bouchard, S. J. Hsu, M. L. Palmeri, N. C. Rouze, K. R. Nightingale, and G. E. Trahey, "Acoustic radiation force-driven assessment of myocardial elasticity using the displacement ratio rate (DRR) method," *Ultrasound Med. Biol.*, vol. 37, no. 7, pp. 1087–1100, Jul. 2011.

[18] M. Couade *et al.*, "In vivo quantitative mapping of myocardial stiffening and transmural anisotropy during the cardiac cycle," *IEEE Trans. Med. Imag.*, vol. 30, no. 2, pp. 295–305, Feb. 2011.

[19] C. Pislaru, M. W. Urban, S. V Pislaru, R. R. Kinnick, and J. F. Greenleaf, "Viscoelastic properties of normal and infarcted myocardium measured by a multifrequency shear wave method: comparison with pressure-segment length method," *Ultrasound Med. Biol.*, vol. 40, no. 8, pp. 1785–1795, Aug. 2014.

[20] M. Pernot, K. Fujikura, S. D. Fung-Kee-Fung, and E. E. Konofagou, "ECG-gated, mechanical and electromechanical wave imaging of cardiovascular tissues in vivo," *Ultrasound Med. Biol.*, vol. 33, no. 7, pp. 1075–1085, Jul. 2007.

[21] J. Provost, W.-N. Lee, K. Fujikura, and E. E. Konofagou, "Electromechanical wave imaging of normal and ischemic hearts in vivo," *IEEE Trans. Med. Imag.*, vol. 29, no. 3, pp. 625–635, Mar. 2010.

[22] J.-Y. Lu and J. F. Greenleaf, "Pulse-echo imaging using a nondiffracting beam transducer," *Ultrasound Med. Biol.*, vol. 17, no. 3, pp. 265–281, Jan. 1991.

[23] L. Sandrin, S. Catheline, M. Tanter, X. Hennequin, and M. Fink, "Time-resolved pulsed elastography with ultrafast ultrasonic imaging," *Ultrason. Imag.*, vol. 21, no. 4, pp. 259–272, Oct. 1999.

[24] L. Tong, H. Gao, H. F. Choi, and J. D'hooge, "Comparison of conventional parallel beamforming with plane wave and diverging wave imaging for cardiac applications: A simulation study," *IEEE Trans. Ultrason., Ferroelectr., Freq. Control*, vol. 59, no. 8, pp. 1654–1663, Aug. 2012.

[25] I. K. Ekroll, A. Swillens, P. Segers, T. Dahl, H. Torp, and L. Lovstakken, "Simultaneous quantification of flow and tissue velocities based on multi-angle plane wave imaging," *IEEE Trans. Ultrason., Ferroelectr., Freq. Control*, vol. 60, no. 4, pp. 727–738, Apr. 2013.

[26] M. Couade *et al.*, "Ultrafast imaging of the heart using circular wave synthetic imaging with phased arrays," in *Proc. IEEE Int. Ultrason. Symp.*, 2009, pp. 515–518.

[27] P. Song *et al.*, "Improved shear wave motion detection using pulse-inversion harmonic imaging with a phased array transducer," *IEEE Trans. Med. Imag.*, vol. 32, no. 12, pp. 2299–2310, Dec. 2013.

[28] C. Papadacci, M. Pernot, M. Couade, M. Fink, and M. Tanter, "High-contrast ultrafast imaging of the heart.," *IEEE Trans. Ultrason., Ferroelectr., Freq. Control*, vol. 61, no. 2, pp. 288–301, Feb. 2014.

[29] T. A. Whittingham, "Tissue harmonic imaging," *Eur. Radiol.*, vol. 9, no. Suppl. 3, pp. S323–S326, Jan. 1999.

[30] F. Tranquart, N. Grenier, V. Eder, and L. Pourcelot, "Clinical use of ultrasound tissue harmonic imaging," *Ultrasound Med. Biol.*, vol. 25, no. 6, pp. 889–894, 1999.

[31] T. Christopher, "Finite amplitude distortion-based pulse echo ultrasonic imaging," *IEEE Trans. Ultrason., Ferroelectr., Freq. Control*, vol. 44, no. 1, pp. 125–139, Jan. 1997.

[32] Q. Ma, Y. Ma, X. Gong, and D. Zhang, "Improvement of tissue harmonic imaging using the pulse-inversion technique," *Ultrasound Med. Biol.*, vol. 31, no. 7, pp. 889–894, Jul. 2005.

[33] J. R. Doherty, J. J. Dahl, and G. E. Trahey, "Harmonic tracking of acoustic radiation force-induced displacements," *IEEE Trans. Ultrason., Ferroelectr., Freq. Control*, vol. 60, no. 11, pp. 2347–2358, Nov. 2013.

[34] J. A. Jensen, S. I. Nikolov, K. L. Gammelmark, and M. H. Pedersen, "Synthetic aperture ultrasound imaging," *Ultrasonics*, vol. 44, no. Suppl. 1, pp. e5–15, Dec. 2006.

[35] G. Montaldo, M. Tanter, J. Bercoff, N. Benech, and M. Fink, "Coherent plane-wave compounding for very high frame rate ultrasonography and transient elastography," *IEEE Trans. Ultrason., Ferroelectr., Freq. Control*, vol. 56, no. 3, pp. 489–506, Mar. 2009.

[36] S. I. Nikolov, J. Kortbek, and J. A. Jensen, "Practical applications of synthetic aperture imaging," in *Proc. IEEE Int. Ultrason. Symp.*, 2010, pp. 350–358.

[37] J. Luo and E. Konofagou, "A fast normalized cross-correlation calculation method for motion estimation," *IEEE Trans. Ultrason., Ferroelectr., Freq. Control*, vol. 57, no. 6, pp. 1347–1357, Jun. 2010.

[38] J. Provost, A. Gambhir, J. Vest, H. Garan, and E. E. Konofagou, "A clinical feasibility study of atrial and ventricular electromechanical wave imaging," *Heart Rhythm*, vol. 10, no. 6, pp. 856–862, Jun. 2013.

[39] J. McLaughlin and D. Renzi, "Using level set based inversion of arrival times to recover shear wave speed in transient elastography and supersonic imaging," *Inverse Prob.*, vol. 22, no. 2, pp. 707–725, 2006.

[40] T. Deffieux, J.-L. Gennisson, B. Larrat, M. Fink, and M. Tanter, "The variance of quantitative estimates in shear wave imaging: Theory and experiments," *IEEE Trans. Ultrason., Ferroelectr., Freq. Control*, vol. 59, no. 11, pp. 2390–2410, Nov. 2012.

[41] E. E. Konofagou and J. Provost, "Electromechanical wave imaging for noninvasive mapping of the 3D electrical activation sequence in canines and humans in vivo," *J. Biomech.*, vol. 45, no. 5, pp. 856–864, Mar. 2012.

[42] H. Kanai, "Propagation of spontaneously actuated pulsive vibration in human heart wall and in vivo viscoelasticity estimation," *IEEE Trans. Ultrason., Ferroelectr., Freq. Control*, vol. 52, no. 11, pp. 1931–1942, Nov. 2005.

[43] C. Papadacci, M. Pernot, M. Couade, M. Fink, and M. Tanter, "Shear Wave Imaging of the heart using a cardiac phased array with coherent spatial compound," in *Proc. IEEE Int. Ultrason. Symp.*, Oct. 2012, pp. 2023–2026.

[44] B. Denarie, T. A. Tangen, I. K. Ekroll, N. Rolim, H. Torp, and T. Bjåstad, "Coherent plane wave compounding for very high frame rate ultrasonography of rapidly moving targets," *IEEE Trans. Med. Imag.*, vol. 32, no. 7, pp. 1265–1276, Jul. 2013.

Mafalda Correia was born in Lisbon, Portugal, on October 1989. She received the B.Sc. and M.Sc. degrees in biomedical engineering from Faculdade De Ciências E Tecnologia (FCT)—Nova University of Lisbon, Lisbon, Portugal, in 2010 and 2012, respectively, and the M.Sc. degree in medical imaging from Telecom ParisTech School, Paris, France, in 2013. She is currently working at the Institut Langevin, in Paris, pursuing the Ph.D. degree, focusing on 2-D and 3-D ultrafast imaging, specifically, on cardiac shear wave elastography.

Jean Provost was born in Montreal, QC, Canada, in 1983. In 2006 and 2009, he completed his undergraduate and graduate studies at Ecole Polytechnique de Montreal, Canada, and Ecole Centrale Paris and Universite Paris-Sud, France, before obtaining the Ph.D. degree in biomedical engineering from Columbia University in New York in 2012.

He is currently a Researcher with the Institut Langevin, Paris, France, and the National Center for Scientific Research (CNRS), Paris, France. His research interests include high-frame-rate ultrasound imaging, tissue motion and blood flow mapping, and multiwave imaging techniques.

Simon Chatelin was born in Orléans, France, in October 1984. He received the Engineer degree in biophysics from Telecom Physics Strasbourg, Strasbourg, France, in 2007, and the Ph.D. degree in biomechanics from the University of Strasbourg, Strasbourg, France, in 2010, for his work on the coupling of biomechanics and medical imaging for the investigation of the intracerebral traumatic brain injuries.

He was a Postdoctoral Fellow with the Center for Research on Inflammation (Inserm-APHP), Paris, France, from 2011 to 2013, and with the Institut Langevin (ESPCI, Inserm), Paris, France, from 2013 to 2015, where he focused on the development of magnetic resonance elastography (MRE) to investigate the cerebral effects of the cannabinoids and on the application of ultrasound shear-wave elastography to muscular and cardiac soft tissues. In March 2015, he joined the Institute of Image-Guided Surgery of Strasbourg (IHU, ICube Laboratory), Strasbourg, France, working on the development of MRE in the field of the numerical simulations dedicated to computer-assisted surgery.

Olivier Villemain was born in Paris, France, in June 1985. He received the M.D. degree in cardiology and the M.Sc. degree in cardiovascular physiology from the University of Paris V, Paris, France, in 2014 and 2015, respectively. He is currently pursuing the Ph.D. degree from the French National Institute of Health and Medical Research (INSERM), Langevin Institute, Paris, France.

His research interests include ultrasound imaging, shear-wave elasticity imaging, and medical ultrasound therapy, specifically on cardiac applications.

Mickael Tanter received an engineering degree in 1994 from Supelec and the Ph.D. degree in physics in 1999 from the Paris 7 University. He is a Research Professor with the French National Institute for Health and Medical Research (INSERM), Langevin Institute, Paris, France. For eight years, he was the Head of the Inserm Laboratory U979, Wave Physics for Medicine, Langevin Institute, ESPCI Paris, France. In 2006, he cofounded Supersonic Imagine, Aix-en-Provence, France, with M. Fink, J. Souquet, and C. Cohen-Bacrie, which is an innovative French company positioned in the field of medical ultrasound imaging and therapy. He is the author of more than 160 peer-reviewed papers and book chapters and holds 24 world patents in the field of ultrasound. His research interests include the development of new approaches in wave physics for medical imaging and therapy, also a wide range of topics: elastography using supersonic shear-wave imaging, ultrafast ultrasound imaging, HIFU, and, more recently, the concept of fUtrasound (functional ultrasonic imaging of brain activity).

Prof. Tanter is an Associate Editor of the IEEE TRANSACTIONS ON ULTRASONICS, FERROELECTRICS, AND FREQUENCY CONTROL, and a member of the Technical Program Committee of the IEEE International Ultrasonics Symposium and the Administrative Committee of the IEEE UFFC Society. He was the recipient of ten scientific awards, including the Frederic Lizzi Early Career Award of the International Society of Therapeutic Ultrasound, the Montgolfier Prize of the French National Society for Industry Valorization, the Leon Brillouin Prize of the Institute of Electrical and Electronics Engineers (IEEE) and SEE Society, the Yves Rocard Prize of the French Society of Physics (SFP), the Sylvia Sorkin Greenfield Award of the American Association of Physicists in Medicine for the Best Paper published in Medical Physics in 2011, the Grand Prize of Medicine and Medical Research of the City of Paris, the Honored Lecture of the Radiology Society of North America in 2012, and the prestigious European Research Council (ERC) Advanced Grant to develop fUltrasound applications.

Mathieu Pernot received an engineering degree in 2001 from the ESPCI in Paris and the Ph.D. degree in physics in 2004 from the Paris 7 University. He is a Research Scientist with the French National Health Institute (INSERM), Paris, France, and a Permanent Member of the Wave Physics for Medicine and Biology team, Institut Langevin, Paris, France, since 2007. He cofounded the French startups Cardiawave, Paris, France, in 2014, and Neuroflows in 2016. He has authored/coauthored about 70 papers in international peer reviewed journals and has filed 17 patents in the field of ultrasound imaging and therapy. His research interests include the development of ultrafast ultrasound imaging and therapeutic ultrasound with a special interest on cardiovascular applications.

Dr. Pernot, as a Principal Investigator, has raised over 3 million euros from the European Research Council, the French National Research Agency, and the French Innovation Program in ultrasound imaging and therapy. He received a prestigious award from the European Research Council (1.5 M€ ERC Starting Grant) in 2012 for his research on ultrafast imaging of the human heart and early diagnosis of heart failure.